Infrared photovoltaic detector based on p-GeTe/n-Si heterojunction

Yiqun Zhao
Beijing University of Technology
Libin Tang (scitang@163.com)
Kunming Institute of Physics
Shengyi Yang
Beijing University of Technology
Shu Ping Lau
Hong Kong Polytechnic University
Kar Seng Teng
Swansea University

Nano Express

Keywords: GeTe, Heterojunction, Optoelectronic characteristics, Photovoltaic detector

Posted Date: May 1st, 2020

DOI: https://doi.org/10.21203/rs.2.24142/v2

Version of Record: A version of this preprint was published on June 29th, 2020. See the published version at https://doi.org/10.1186/s11671-020-03336-7.

Abstract

GeTe is an important narrow bandgap semiconductor material and has found application in the fields of phase change storage as well as spintronics devices. However, it has not been studied for application in the field of infrared photovoltaic detectors working at room temperature. Herein, GeTe nanofilms were grown by magnetron sputtering technique and characterized to investigate its physical, electrical and optical properties. A high-performance infrared photovoltaic detector based on GeTe/Si heterojunction with the detectivity of 8×10 11 Jones at 850 nm light irradiation at room temperature was demonstrated.

Background

There has been a great interest in infrared detectors due to its many potential applications in night vision imaging, safety, remote sensing, food inspection, biology and other fields [1-3]. Generally, photovoltaic infrared detectors take advantage of minority carrier effects leading to short response time, which is ideal for imaging and sensing applications. HgCdTe based infrared detector is well established [4, 5]. However, the lattice mismatch of HgCdTe and Si does not permit integration of detection and data processing units, hence resulting in costly system and hindering miniaturization of the technology.

There has been much research activities in developing various heterogeneous structures based on two-dimensional materials grown on different substrates [6-9]. The resultant heterogeneous structure depends on van der Waals interaction [10] and there is no requirement for lattice matching of the different materials.

GeTe material has attracted extensive attention in recent years [11-15]. It has been considered as a strong contender for the next-generation memory technology as the material exhibits different physical, electrical and optical properties when it is in amorphous and crystal phases [16-21]. GeTe can also be made into dilute magnetic semiconductor, which is an important material for spintronics devices [15, 22, 23]. If the unique storage and computing features of GeTe can be integrated to develop novel devices, this will lead to significant advancement in the computing technology.

Furthermore, the ability to develop photovoltaic detector based on two-dimensional GeTe and Si heterojunction will lead to groundbreaking technology due to their compatibility with Si circuit and GeTe-based spintronic device processes. It will facilitate seamless and fast connection involving photovoltaic detectors in the field of computing in the future. Importantly, the technology is suitable for miniaturization at low cost.

In this work, p-type GeTe nanofilms were prepared by magnetron sputtering and annealing methods. The physical, electronic and optical properties of the nanofilms were investigated. Finally, a photovoltaic detector based on p-GeTe/n-Si heterojunction was fabricated and its performance was characterized.

Methods

The device was fabricated using the following processes. First, a n-type monocrystalline silicon (Si) substrate was cleaned by chemical bath method using a mixed solution containing H_2O: H_2O_2: NH_3 H_2O (3: 1: 1) at 80 ℃ for 30 min and dried under air flow. GeTe film was then deposited by magnetron sputtering directly onto the cleaned substrate at a pressure of 5 Pa for 120 s from an initial vacuum of 6.0×10^{-4} Pa. Subsequently, the film was wrapped in copper foil and then annealed in a vacuum oven at 360 ℃ for 10 min. The annealing method was based on preliminary experiments and previously reported phase transition temperature of the material in the literatures [18, 24-26]. Finally, a pair of aluminum (Al) electrodes was evaporated onto the GeTe film and Si substrate using physical vapor deposition (PVD) technique (at a pressure of 7.0×10^{-5} Pa) through a shadow mask. The thickness of the Al electrodes was approximately 100 nm as measured by a quartz oscillator during deposition The effective area of the device was 1.5 mm^2. Fig. 1 (a) and (b) illustrate the magnetron sputtering and oven annealing processes, respectively. Fig. 1 (c) and (d) show the as-deposited and annealed GeTe films, respectively.

Results And Discussion

High-resolution transmission electron microscopy (HRTEM) images of the annealed GeTe film are shown in Fig. 1 (e) and (f). The insets show the Fast Fourier transform (FFT) patterns of the GeTe film. Indices of crystal planes are indicated on the images. According to these results, the annealed GeTe film exhibited good crystallinity. Fig. 1 (g) shows the line profiles of the lattice fringes shown in Fig. 1 (e) and (f). The top and bottom line profiles of Fig. 1 (g) corresponds to (202) and (220) crystal planes of GeTe film, which has a lattice fringe separation of 0.294 and 0.209 nm, respectively. Schematic diagram of the GeTe lattice structure is illustrated in Fig. 1 (h). Fig. 1 (i) and (j) show crystal plane models of GeTe as observed in Fig. 1 (e) and (f), respectively.

Raman spectroscopy was performed to study the structure of the GeTe films before and after annealing using a Renishaw inVia Raman microscope equipped with an argon-ion laser operating at an excitation wavelength of 514 nm. Fig. 2 (a) and (b) show the normalized Raman spectra of as-deposited and annealed GeTe films, respectively. The results are in good agreement with the literatures [27, 28]. There were three distinctive bands between 100 and 300 cm^{-1} as shown in Fig. 2 (a). These bands were situated at 124.8, 161.8 and 223.5 cm^{-1}, namely band B, C and D, respectively. After annealing, there was a significant reduction in band D and also an appearance of band A situated at 108.1 cm^{-1} as shown in Fig. 2 (b). Band B, C and D were also red-shifted by 1.1, 5.3, and 21.9 cm^{-1},respectively. These are attributed to structural transformation of the GeTe film resulting in reduction in the degree of disorder (e.g. ratio of intermolecular to intramolecular interactions) [27].

To investigate the optical properties of the GeTe films before and after annealing, UV-Vis-NIR absorption spectroscopy were performed using a Horiba iHR 320 spectrometer. Fig. 2 (c) shows the UV-Vis-NIR absorption spectra obtained from both films. An absorption peak at 600 nm was apparent after

annealing. The absorption coefficient of annealed GeTe film was significantly larger than that of unannealed film. Furthermore, a decreasing trend in the absorption coefficient was observed for an increasing wavelength in the infrared band. Bandgap energy (E_g) of the films can be determined using the following formulae [29, 30]: (see Formula 1 in the Supplementary Files)

where hv is energy of incident photon, α is optical absorption coefficient associated with hv, and C is a constant. The direct optical bandgap of the GeTe films can be estimated from the curve of α^2 vs. photon energy (hv) as shown in the inset of Fig. 2 (c). It can vary greatly depending on the experimental conditions and theoretical models [31]. In this work, the estimated E_g of the GeTe films before and after annealing was 0.85 and 0.70 eV, respectively. This is in good agreement with previous work performed by others, which reported an optical bandgap of ~ 0.85 eV for an amorphous GeTe film and ~ 0.73 - 0.95 eV for crystalline film [32]. A reduction of E_g was reported after annealing because of long-range ordering of the lattice.

Atomic force microscopy (AFM) was carried out to determine the thickness of the films using AFM (SPA-400). Photoresist mask was used to prepare the sample for AFM measurements. Fig. 2 (d) shows an optical image of the prepared sample for AFM with an obvious boundary between GeTe film and substrate. Fig. 2 (e) reveals a film thickness of 33 ± 1.5 nm on Si substrates after annealing. Annealing has a little effect on the root-mean-square (RMS) surface roughness of the GeTe thinfilms, the RMS surface roughness decreased from 2.1 nm (as-deposited GeTe) to 1.4 nm (annealed GeTe).

The effect of annealing on the structure of GeTe nanofilms was further investigated using X-ray diffraction (XRD). Fig. 2 (f) shows the XRD spectra of the as-deposited (blue) and annealed (red) GeTe nanofilms. Two strong diffraction peaks at 29.9 ° and 43.2 °, which corresponded to (202) and (220) lattice planes respectively, appeared after annealing. In addition, two weak diffraction peaks at 26.0 ° and 53.5 °, which corresponded to (021) and (042) lattice planes respectively, also appeared in the spectrum. When combined with the above TEM results, it is evident that the GeTe nanofilm preferentially ordered along (220) and (202) lattice planes during the annealing process. Compared to the as-deposited GeTe films, the annealed GeTe has a drastic change in the crystal phase, the difference in the structure-related optical properties (absorption spectra) is shown in Fig. 2 (f) and Fig. 2 (c).

Elemental composition and chemical bonds at the surface of annealed GeTe nanofilms were studied by X-ray photoelectron spectroscopy (XPS) using AlKα radiation with energy of 1486.6 eV. XPS spectra of Ge 2p, Ge 3d and Te 3d core level peaks of the annealed GeTe film are shown in Fig. 2 (g), (h) and (i), respectively. The Ge 2p core level consisted mainly of Ge $2p_{3/2}$ (1220.1 eV) and Ge $2p_{1/2}$ (1251.1 eV) doublet peaks. The Ge 3d core level was deconvoluted into two components, namely Ge-Te and Ge-O at binding energy of 30.0 and 32.8 eV, respectively. The Te 3d core level consisted of Ge-Te, Te-O and Te-Te components. The Te-O (Te^{4+}) peaks at 576.5 eV (Te $3d_{5/2}$) and 587.0 eV (Te $3d_{3/2}$) in Fig. 2 (i) were associated with TeO_2 [33, 34]. Both Ge 3d and Te 3d core levels of annealed GeTe nanofilm exhibited oxygen-related components as shown in Fig. 2 (h) and (i), respectively. However, there was no oxygen-related component at Ge 2p core level, which was at greater penetration depth, as shown in Fig. 2 (g).

Furthermore, GeO_2 and TeO_2 were absent from the XRD and TEM characterizations, hence this suggests that the oxidation of Ge and Te atoms were primarily localized at the surface of the film by atmospheric oxygen during the transfer and annealing processes [34] and the oxide layer was

A prototype photovoltaic detector based on p-GeTe/n-Si heterojunction was fabricated to explore the use of the material in the field of optoelectronics. The device fabrication processes are illustrated in Fig. 3 (a). Fig. 3 (b) depicts the structure of the photodetector. The thickness of the GeTe film and Al electrodes was 33 and 100 nm, respectively. Fig. 3 (c) and (d) show the response time of the device. The rise time (t_R) is defined as time taken for the current to increase from 10 to 90 % of the peak, while the decay time (t_D) is time taken for current to decrease from 90 to 10 %. As shown, the rise and fall time were symmetrical with a response time (τ) of 134 ms (e.g. (t_R+ t_D)/2).

Photoresponse of the device was evaluated from *J-V* measurements using Keithley 2400 sourcemeter under light illumination. The log *J* vs *V* characteristics of the device irradiated by λ=850 nm light at different densities of 20, 53, and 90 μW•cm^{-2} and under dark condition performed at room temperature are shown in Fig. 3 (e). It can be seen from Fig. 3 (e) that the voltage corresponding to the minimum value of J_{opt} (i.e. photocurrent density) deviated by 0.1 V from the voltage corresponding to the minimum value of J_D (i.e. dark current density) in the direction of positive bias, and that the photogenic voltage was generated under the light conditions. Therefore, the p-GeTe/n-Si heterojunction has demonstrated its potential application in infrared detection.

Two important figures of merit for photodetector, such as responsivity (*R*) and detectivity (D^*), were determined using the following equations [35, 36]: (see Formulas 2 and 3 in the Supplementary Files)

where I_p is photocurrent that equals to absolute value of current under irradiation subtracting that in the dark, *A* is the effective area of the device, P_{opt} is incident optical power, I_d is dark current and *q* is unit charge (1.6×10^{-19} C).

The values of *R* and D^* were 6 - 15 A/W and 1 - 8×10^{11} Jones (1 Jones =1 cm•Hz$^{1/2}$W^{-1}) as obtained from Fig. 3 (f) and (g), respectively. The device was evaluated at room temperature, unpackaged and without optimization. Table 1 lists the responsivity and detectivity of some infrared photodetectors based chalcogenide/Si heterojunction, it can be seen that GeTe/Si shows a relatively higher performance at room temperature, which maybe due to the big absorption coefficient and the direct band gap of GeTe.

Table 1 Comparison of responsivity and detectivity of infrared photodetectors based on other materials forming heterojunction with Si

Heterojunction	Wavelength (nm)	R (A/W)	D^* (Jones)	Ref.
GeTe/Si	850	6 - 15	$1 - 8\times10^{11}$	This work
Bi_2Se_3/Si	808	24.28	4.4×10^{12}	[37]
SnS/Si	850	0.083	5.3×10^{9}	[38]
MoS_2/Si	300-1100	0.0119	2.1×10^{10}	[39]
WS_2/Si	400-1100	1.11	5×10^{11}	[40]
WS_2/Si	Near-infrared	3.7-4.5		[41]

Conclusions

Crystalline GeTe nanofilms were produced by magnetron sputtering and post-annealing treatment. The physical, electronic and optical properties of the nanofilms before and after annealing were studied. After annealing at 360 ℃, the nanofilm revealed long-range order and bandgap energy of 0.70 eV. Photovoltaic detector based on the p-GeTe/n-Si heterojunction was fabricated and demonstrated photoresponse at 850 nm irradiation exhibiting high R of 6 - 15 A/W and D* of $1 - 8\times10^{11}$ Jones with a response time of 134 ms. Hence, the use of p-GeTe/n-Si heterojunction in infrared detection was demonstrated in this work. It has enormous potential for integration with other fields, such as computing and data storage.

Abbreviations

PVD: Physical vapor deposition; TEM: Transmission electron microscope; HRTEM: High-resolution transmission electron microscope; FFT: Fast Fourier transform; AFM: Atomic force microscope; XRD: X-ray diffractometer; XPS: X-ray photoelectron spectroscopy

Declarations

Acknowledgements

This work was supported by National Natural Science Foundation of China (Grant Nos. 61106098, and 51462037); Key Project of Applied Basic Research of Yunnan Province, China (Grant No. 2012FA003); PolyU grants (1-ZVGH and 1-BBAD); Research Grants Council of Hong Kong (Project Nos.: PolyU 153030/15P, PolyU 153271/16P, and PolyU 153039/17P).

Availability of Data and Materials

The conclusions made in this manuscript are based on the data (main text and figures) presented and shown in this paper.

Authors' Contributions

YZ carried out the experiments and drafted the manuscript. LT designed the experiments. LT and SY supervised the experiments. KST, and SPL participated in the discussion and analyzed the experimental results. LT, KST, and SPL helped to draft and revise the manuscript. All authors read and approved the final manuscript.

Competing Interests

The authors declare that they have no competing interests.

Publisher's Note

Springer Nature remains neutral with regard to jurisdictional claims in published maps and institutional affiliations.

Author details

[1]School of Physics, Beijing Institute of Technology, Beijing 100081, China

[2] Kunming Institute of Physics, Kunming 650223, China

[3] Yunnan Key Laboratory of Advanced Photoelectric Materials and Devices, Kunming 650223, China

[4]Kunming Metallurgy College, Kunming 650033, China

[5]Department of Applied Physics, The Hong Kong Polytechnic University, Hong Kong SAP, P.R. China

[6]College of Engineering, Swansea University, Bay Campus, Fabian Way, Swansea SA1 8EN, United Kingdom.

References

1. Abbas MM, Kostiuk T, Ogilvie KW (1976) Infrared upconversion for astronomical applications. Appl Opt 15: 961-970
2. Tan MC, Al-Baroudi L, Riman RE (2011) Surfactant effects on efficiency enhancement of infrared-to-visible upconversion emissions of $NaYF_4$:Yb-Er. ACS Appl Mater Interfaces 3: 3910-3915
3. Ring EF, Ammer K (2012) Infrared thermal imaging in medicine. Physiol Meas 33: R33-46
4. Rogalski A, Martyniuk P, Kopytko M (2019) Type-II superlattice photodetectors versus HgCdTe photodiodes. Progress in Quantum Electronics : 100228
5. Kopytko M, Rogalski A (2016) HgCdTe barrier infrared detectors. Progress in Quantum Electronics 47: 1-18
6. Gan X, Shiue R-J, Gao Y et al (2013) Chip-integrated ultrafast graphene photodetector with high responsivity. Nature Photonics 7: 883

7. Wang X, Cheng Z, Xu K et al (2013) High-responsivity graphene/silicon-heterostructure waveguide photodetectors. Nature Photonics 7: 888-891
8. Gan X, Gao Y, Fai Mak K et al (2013) Controlling the spontaneous emission rate of monolayer MoS_2 in a photonic crystal nanocavity. Appl Phys Lett 103: 181119
9. Sobhani A, Lauchner A, Najmaei S et al (2014) Enhancing the photocurrent and photoluminescence of single crystal monolayer MoS_2 with resonant plasmonic nanoshells. Appl Phys Lett 104: 031112
10. Wang L, Meric I, Huang PY et al (2013) One-dimensional electrical contact to a two-dimensional material. Science 342: 614-617
11. Zhang D, Zhou Z, Wang H et al (2018) Tunable Electric Properties of Bilayer α-GeTe with Different Interlayer Distances and External Electric Fields. Nanoscale Res Lett 13
12. Kolobov AV, Krbal M, Fons P et al (2011) Distortion-triggered loss of long-range order in solids with bonding energy hierarchy. Nat Chem 3: 311-316
13. Zhang J, Huang R, Shi L et al (2013) Bi doping modulating structure and phase-change properties of GeTe nanowires. Appl Phys Lett 102: 063104
14. Wang L, Yang CH, Wen J et al (2016) Overview of Probe-based Storage Technologies. Nanoscale Res Lett 11: 342
15. Hoffmann A, Bader SD (2015) Opportunities at the Frontiers of Spintronics. Phys Rev Applied 4: 047001
16. Kooi BJ, Momand J (2019) High Resolution Imaging of Chalcogenide Superlattices for Data Storage Applications: Progress and Prospects. physica status solidi (RRL) – Rapid Research Letters 13: 1800562
17. Meena J, Sze S, Chand U et al (2014) Overview of emerging nonvolatile memory technologies. Nanoscale Res Lett 9: 526
18. Siegrist T, Jost P, Volker H et al (2011) Disorder-induced localization in crystalline phase-change materials. Nat Mater 10: 202-208
19. Zhang W, Mazzarello R, Wuttig M et al (2019) Designing crystallization in phase-change materials for universal memory and neuro-inspired computing. Nature Reviews Materials 4: 150-168
20. Wuttig M, Yamada N (2007) Phase-change materials for rewriteable data storage. Nat Mater 6: 824
21. Wang L, Lu S-R, Wen J (2017) Recent Advances on Neuromorphic Systems Using Phase-Change Materials. Nanoscale Res Lett 12: 347
22. Rinaldi C, Varotto S, Asa M et al (2018) Ferroelectric Control of the Spin Texture in GeTe. Nano Lett 18: 2751-2758
23. Manchon A, Koo HC, Nitta J et al (2015) New perspectives for Rashba spin-orbit coupling. Nat Mater 14: 871-882
24. Ren K, Zhu M, Song W et al (2019) Electrical switching properties and structural characteristics of GeSe-GeTe films. Nanoscale 11: 1595-1603

25. Carria E, Mio AM, Gibilisco S et al (2011) Amorphous-Crystal Phase Transitions in Ge_xTe_{1-x} Alloys. J Electrochem Soc 159: H130-H139
26. Chua EK, Shi LP, Zhao R et al (2010) Low resistance, high dynamic range reconfigurable phase change switch for radio frequency applications. Appl Phys Lett 97: 183506
27. Andrikopoulos KS, Yannopoulos SN, Voyiatzis GA et al (2006) Raman scattering study of the a-GeTe structure and possible mechanism for the amorphous to crystal transition. J Phys: Condens Matter 18: 965-979
28. Sarkar D, Sanjeev G, Mahesha MG (2015) Analysis of electron beam-induced effect on electrical switching properties of glass chalcogenide GeTe thin films through Raman spectroscopy. Appl Phys A 119: 49-54
29. Manser JS, Christians JA, Kamat PV (2016) Intriguing Optoelectronic Properties of Metal Halide Perovskites. Chem Rev 116: 12956-13008
30. Tauc J, Menth A (1972) States in the gap. J Non-Cryst Solids 8-10: 569-585
31. Vadkhiya L, Arora G, Rathor A et al (2011) Electron momentum density and band structure calculations of α- and β-GeTe. Radiat Phys Chem 80: 1316-1322
32. Bahl SK, Chopra KL (1970) Amorphous versus Crystalline GeTe Films. III. Electrical Properties and Band Structure. J Appl Phys 41: 2196-2212
33. Qian H, Tong H, Zhou LJ et al (2016) Low work function of crystalline GeTe/Sb_2Te_3 superlattice-like films induced by Te dangling bonds. J Phys D: Appl Phys 49: 495302
34. Yashina LV, Kobeleva SP, Shatalova TB et al (2001) XPS study of fresh and oxidized GeTe and (Ge,Sn)Te surface. Solid State Ionics Diffusion & Reactions 141: 513-522
35. Yang Y, Dai H, Yang F et al (2019) All-Perovskite Photodetector with Fast Response. Nanoscale Res Lett 14: 192
36. Tan H, Fan C, Ma L et al (2015) Single-Crystalline InGaAs Nanowires for Room-Temperature High-Performance Near-Infrared Photodetectors. Nano-Micro Letters 8: 29-35
37. Zhang H, Zhang X, Liu C et al (2016) High-Responsivity, High-Detectivity, Ultrafast Topological Insulator Bi_2Se_3/Silicon Heterostructure Broadband Photodetectors. ACS Nano 10: 5113-5122
38. Patel M, Kim H-S, Kim J (2017) Wafer-scale production of vertical SnS multilayers for high-performing photoelectric devices. Nanoscale 9: 15804-15812
39. Zhang Y, Yu Y, Mi L et al (2016) In Situ Fabrication of Vertical Multilayered MoS2/Si Homotype Heterojunction for High-Speed Visible-Near-Infrared Photodetectors. Small 12: 1062-1071
40. Chowdhury RK, Maiti R, Ghorai A et al (2016) Novel silicon compatible p-WS_2 2D/3D heterojunction devices exhibiting broadband photoresponse and superior detectivity. Nanoscale 8: 13429-13436
41. Lan C, Li C, Wang S et al (2016) Zener Tunneling and Photoresponse of a WS2/Si van der Waals Heterojunction. ACS Appl Mater Interfaces 8: 18375-18382

Figures

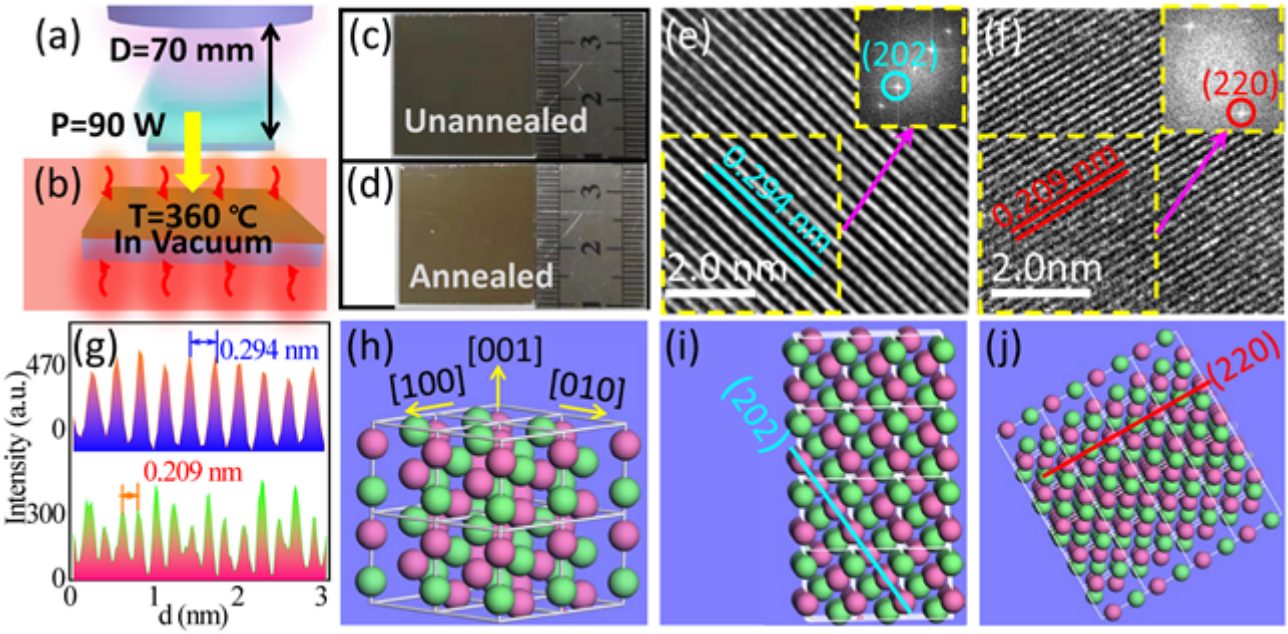

Figure 1

a Magnetron sputtering of GeTe film on Si substrate. b Post-annealing of the GeTe film. c Optical images of as-deposited and d annealed GeTe films on quartz substrate. e-f TEM images and FFT patterns (inset) of the annealed GeTe film. g Line profiles of the lattice fringes of (202) and (220) crystal planes as shown in the top and bottom panels, respectively. h-j Schematic diagrams of the crystal structures.

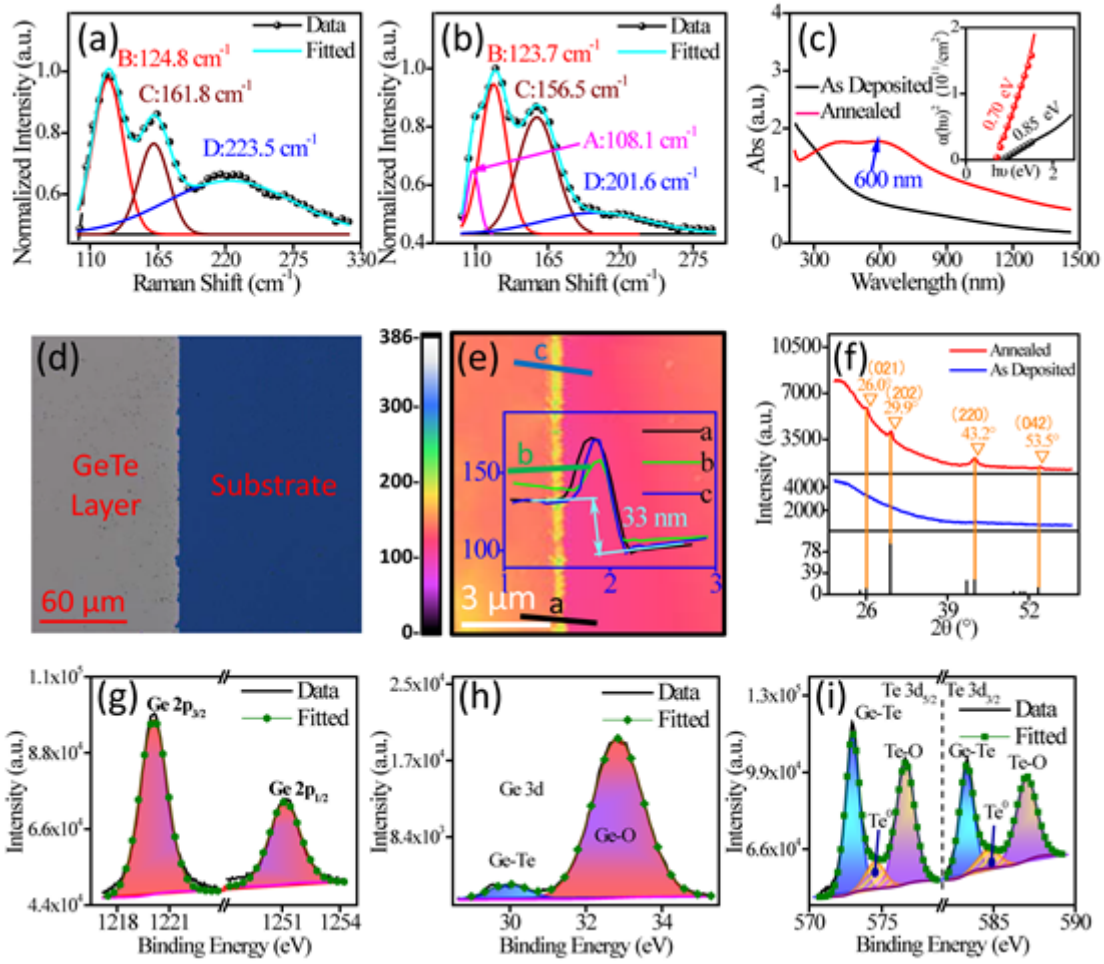

Figure 2

a-b Normalized Raman spectra of GeTe films before and after annealing, respectively. c UV-Vis-NIR absorption spectra of the GeTe films before and after annealing. (Inset) Plot of α2 versus photon energy (hv) of the two GeTe films. d Optical images of the annealed GeTe film for AFM measurement. e AFM image and line profiles (inset) for thickness measurement of the annealed GeTe film. f XRD spectra of the GeTe films before and after annealing. g-i XPS spectra of Ge 2p, Ge 3d and Te 3d core levels of the annealed GeTe film.

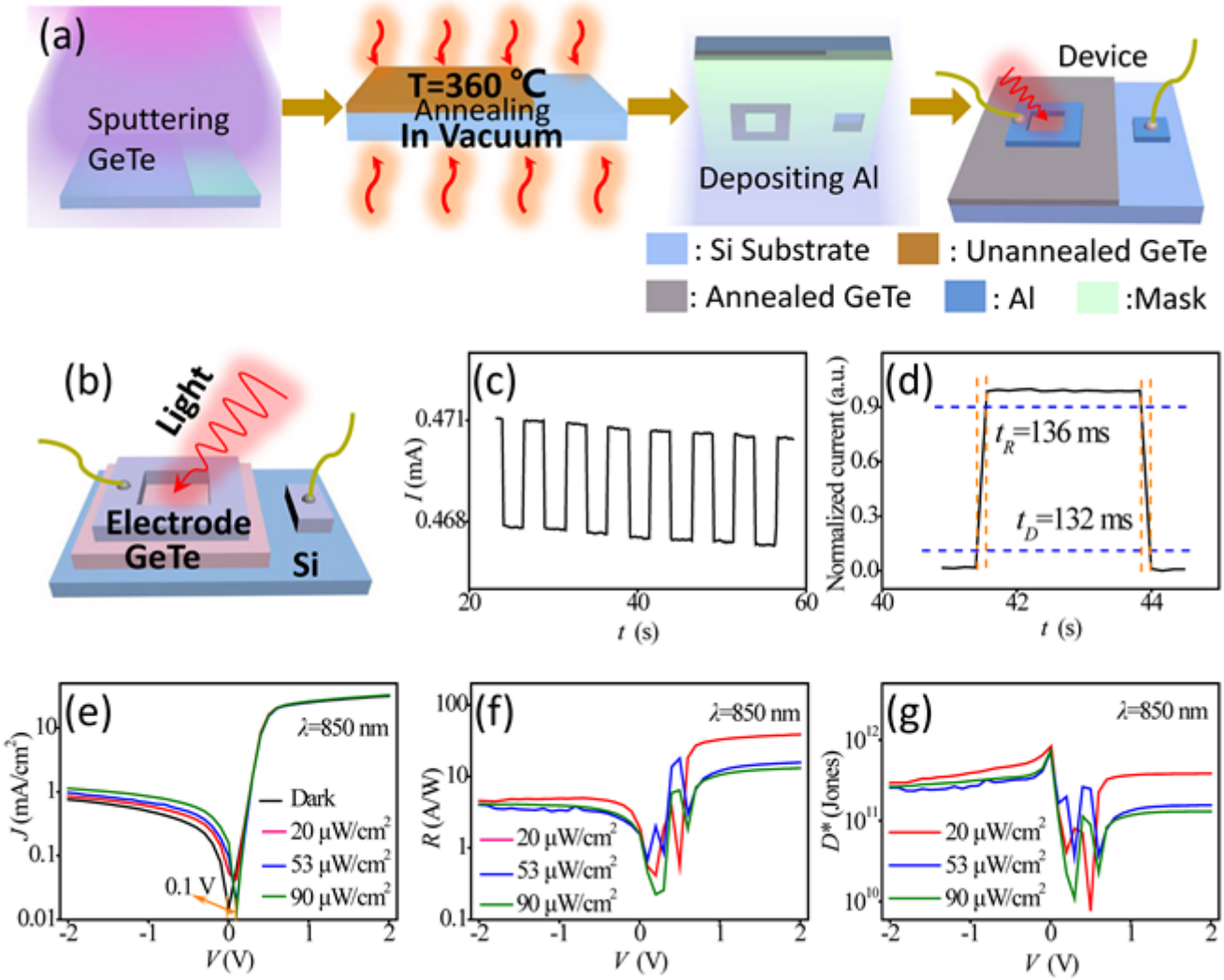

Figure 3

a Schematic diagrams illustrating the fabrication process of photovoltaic detector based on p-GeTe/n-Si and b the device structure. c-d Temporal photoresponse of the device. e log(J)-V characteristics of the photovoltaic detector under dark (black line) and irradiation (other lines). f Plots of R (Responsivity)-V and g D* (Detectivity)-V characteristics of the photovoltaic detector.

Supplementary Files

This is a list of supplementary files associated with this preprint. Click to download.

- Formulas.pdf